



Effects of weave path parameters on the geometry of wire arc additive manufactured features

Jacob Bultman¹ · Christopher Saldaña¹

Received: 3 June 2022 / Accepted: 14 November 2022 / Published online: 15 December 2022
© The Author(s), under exclusive licence to Springer-Verlag London Ltd., part of Springer Nature 2022

Abstract

The present work investigates the effect of process parameters on the geometry of wire arc additive manufactured parts. The geometric accuracy of features produced with a weaving strategy is compared to what can be accomplished with a typical overlapping bead strategy. In this work, single-layer and multi-layer geometries were deposited under varying process and path parameters. The wavelength, amplitude, and torch speed of the weaving path were varied, while the power, wire feed speed, and contact tip to work distance remained constant. The geometric deposition efficiencies of several samples produced with a weave strategy are directly compared to samples generated with two parallel overlapping beads with torch speeds defined to match the deposition rate of the weave samples. Feature geometries were characterized using optical microscopy and laser scanning data. The results indicate that implementing a weave path strategy can improve the geometric accuracy of wire arc additive features, thus increasing the effective volumetric deposition rate of the process. It is shown that the most consistent improvements resulted from the combination of low wavelength and high amplitude, which correlate to wider and taller printed layers.

Keywords Additive manufacturing · Wire arc additive manufacturing · GMAW · Welding

1 Introduction

Wire arc additive manufacturing (WAAM) is a type of directed energy deposition (DED) additive manufacturing process where a power source generates an electric arc to melt a metal wire, or filler material, and deposit the molten metal onto a substrate layer by layer [1]. Many instances of WAAM systems utilize legacy welding technology such as metal inert gas (MIG) or tungsten inert gas (TIG) welders to produce parts. These parts have a significantly lower resolution than parts manufactured via other additive manufacturing processes such as blown powder DED or laser powder bed fusion [2]. However, WAAM has the advantage of being significantly cheaper to use as it has high

deposition rates, low material cost, and is primarily based on well studied and developed technology [1].

Despite the advantages and practical applications of WAAM, it has several drawbacks. High heat input inherent to the process leads to low forming quality as the surface smoothness of features is reduced at high temperatures [3]. Additionally, thermal shrinkage and expansion with cyclical melting and cooling processes cause distortion of the part [4]. Because of this, features produced with WAAM often require large amounts of post process machining to reduce the part to the desired geometry [5]. To alleviate some of this error and obtain better material filling and process time efficiencies, different layer path strategies can be employed. Producing large features has been accomplished by using traditional path strategies which fill areas with overlapping beads via parallel or spiralling tracks laid side by side [6]. The downside is that these tracks must be printed with a small working set of process parameters to maintain the welding mode and avoid causing defects in the beads like humping or lack of fusion. This traditional style of deposition limits the shape of features to what can be made by overlapping an integer number of single-track beads. Such limitations cannot reliably produce true near-net-shape parts. As a solution, research has been conducted on the

✉ Jacob Bultman
jake.bultman@gmail.com

Christopher Saldaña
christopher.saldana@me.gatech.edu

¹ George W. Woodruff School of Mechanical Engineering,
Georgia Institute of Technology, Atlanta, GA, USA

implementation of a deposition path that utilizes a single weaving bead to produce wide features with WAAM.

Several aspects of a weaving path have previously been explored. Hu et al. [7], Chen et al. [8], and He et al. [9] investigated the temperature fields produced during a weaving torch path in WAAM. Hu and Chen found that the heat input in weave beads is evenly distributed across the bead, leading to a reduced maximum temperature. However, Hu concluded that a weaving arc can also enlarge the melt pool causing steeper temperature gradients compared to non-weave beads. He et al. also found the weaving path to produce a more uniform temperature field and a smaller temperature gradient between peak and interlayer temperatures, leading to more synchronous melt pool solidification and reduced stresses. Additionally, Yaseer et al. [10] evaluated the geometric quality of the top surface of WAAM beads with changing weave path parameters. The authors found that higher weaving amplitudes (A) and a wire feed speed (WFS) to torch speed (TS) ratio of 7 cause a reduction in the top surface roughness. Similarly, the effectiveness of WAAM for creating ideal geometric features has been investigated. Ma et al. considered the optimization of weave path inputs to produce features with low top surface roughness [11] as well as to control the height and width of aluminum depositions, especially at locations of intersecting geometries [12]. The authors found the implementation of a weave path to be successful in increasing the top surface flatness of walls. The same study also shows the width of walls to increase and the wall height to decrease with an increase in A and wavelength (λ). However, the results from this study are based on width measurements and calculated heights of single-layer beads and small walls.

While unique torch path strategies are being studied in the context of WAAM as a result of their enhancements for manual welding with respect to geometry and melt pool control, they have also been compared to the typical strategy for producing WAAM features. Usually, a working parameter set for WAAM is selected and multiple beads are overlapped to achieve the desired geometry. Zhan et al. [13, 14] and Guzman-Flores et al. [15] both compared the use of weaving torch path strategies to the use of parallel, overlapping beads to join thick plates of metal. Aldalur et al. [16, 17] compared the top surface quality, tensile strength, hardness, and fracture toughness between walls built with a weave strategy and an overlapping strategy. Finally, the application of a weave strategy was shown to reduce tensile strength and increase elongation in ER70S-6 steel compared to material deposited with overlapping beads due to the formation of larger grains [17]. While some of these studies compare the as-built geometry of WAAM features, the effects of parameters on the overall geometric efficiency and macrostructure of features produced with weave

compared to traditional bead overlap models have not been considered.

The present study seeks to characterize the effects of weave path and welding process parameters on the overall and usable geometry of large WAAM parts. Additionally, a comparison of performance with respect to deposition efficiencies between a weave path and a typical torch path will be made as previous studies lack this information. The purpose of the study is to provide a unique build strategy and parameter set to enhance the potential for WAAM to produce true near-net-shape parts, ultimately requiring the least amount of time and material waste to achieve the desired finished geometry.

2 Methodology

2.1 Process overview

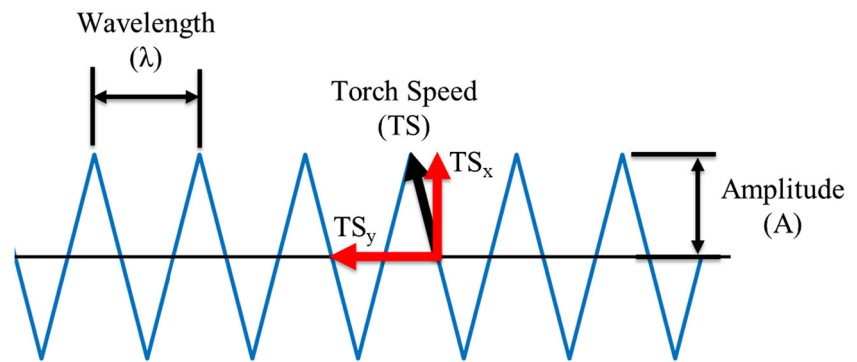
The WAAM depositions were produced using a standard gas metal arc welding (GMAW) process. The walls produced with a weaving strategy utilized the triangular weave path. An example of a triangular path and its associated parameters can be seen in Fig. 1. The TS of weaving paths can be broken down into traverse and transverse directions labeled TS_y and TS_x respectively. For the bead overlap experiments, two parallel beads were deposited side by side for each layer and layers were deposited on top of each other to produce walls. In order to maintain the build quality of walls, a dwell period was introduced between each layer. The goal of the dwell is to allow the deposited feature to cool to below 600°F before depositing the next layer. From previous experiments and experience with the machine and process conditions, an adequate cooling time was determined to be 120 or 180s depending on the heat input as a result of an individual sample's process parameters.

The path strategy for bead overlap experiments is represented in Fig. 2. The arrows in the figure represent the deposition direction of each bead. For all bead overlap experiments in this study, the build direction of beads in each layer was alternated, and the start and end position alternates for each layer to reduce the accumulation of excess material at arc start positions. In the same way as the weave path experiments, a dwell time was added between each layer for multi-layer bead overlap depositions.

2.2 Equipment

The machine used for printing was a Cincinnati Dart 3-axis CNC. The machine was retrofitted with a welder head for WAAM depositions as seen in Fig. 3. The welder was a Lincoln Electric S500 Power Wave with a Lincoln Electric 4R 220 Auto Drive wire feeder. The wire used was

Fig. 1 Triangle weave path deposition strategy



0.045 inch diameter (1.2 mm) ER70S-6 carbon steel with a chemical composition of C-0.08, Cu-0.18, Mn-1.53, P-0.009, Si-0.88, S-0.01 by weight percent. Argon gas was used to shield the welding operation with a constant flow rate of 45 cubic feet per hour or 21.2 liters per minute. for all experiments. This flow rate has been seen to provide good quality beads through previous experiments with this setup. All experiments were performed with a welder power of 2.1 kW as this has been seen to produce desirable build quality through previous experiments. A constant 240 inches/min (6.1 meters/min) WFS was used for all experiments as to ensure a spray transfer weld mode. Each experiment was deposited onto a 1/4 inch (6.35 mm) hot rolled mild steel plate. Finally, a contact tip to work distance of 0.4 inches (10.2 mm) was used across all samples to maintain proper gas shielding and arc current.

For obtaining the 3D scan of weave and bead overlap walls, a laser light scanner attachment on an Edge FaroArm model 14000 was used. To obtain the desired metrics from the single-layer experiments, the samples were ground and polished on a MetaServ 250 to 39.3 microinches ($1\mu m$), etched with a 5% Nital solution, and photographed using a Leica DVM6 optical microscope.

2.3 Design of experiments

2.3.1 Weave parameters

For the weave experiments, samples were deposited at their respective parameters based on nominal settings to maximize deposition rate and achieve complete bead penetration. It was found in preliminary experiments that

TS, λ , and A must be changed together to avoid humping, lack of fusion, and excessive dripping. Thus, a parameter set for the single and multi-layer weave depositions provide quantifiable results for all parameter combinations. A TS of 35 inches/min (0.89 meters/min) was chosen as the lower bound because depositions at lower TSs would result in unacceptably high heat input especially when paired with short λ s. A TS of 55 inches/min (1.40 meters/min) was chosen as the upper bound because higher TSs would result in lack of complete fusion to the build plate and the possibility of straying outside the required conditions for maintaining spray transfer welding mode. Low and high levels of 0.1 and 0.2 inches (2.54 and 5.08 mm) were chosen for λ as shorter λ s resulted in too much heat input, and longer λ s resulted in poor surface quality. Low and high levels of 0.1 and 0.2 inches were chosen for A as smaller As produced geometries that are easily achievable with a single, straight bead, and larger As require short λ s and high TSs.

2.3.2 Overlap parameters

The bead overlap experiment conditions were chosen to coincide with parameter sets from the low λ weave experiment samples. Low λ samples were chosen to match parameters because they seem to provide the best surface quality from preliminary experiments. The TS required for each overlap sample was chosen to match half of the TS_y of the associated weave wall. This was done to provide an equal total path time per layer. The calculation of the TS in terms of weave path parameters is shown in Eq. 1. The overlap spacing for each parameter setting was determined

Fig. 2 Bead overlap path deposition strategy

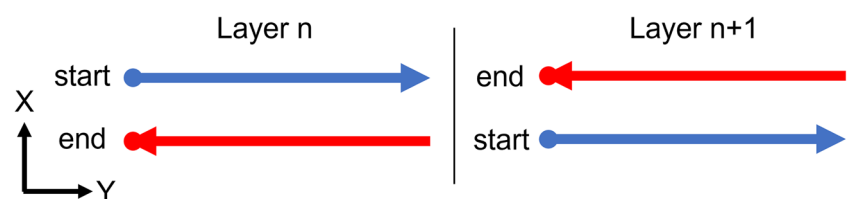
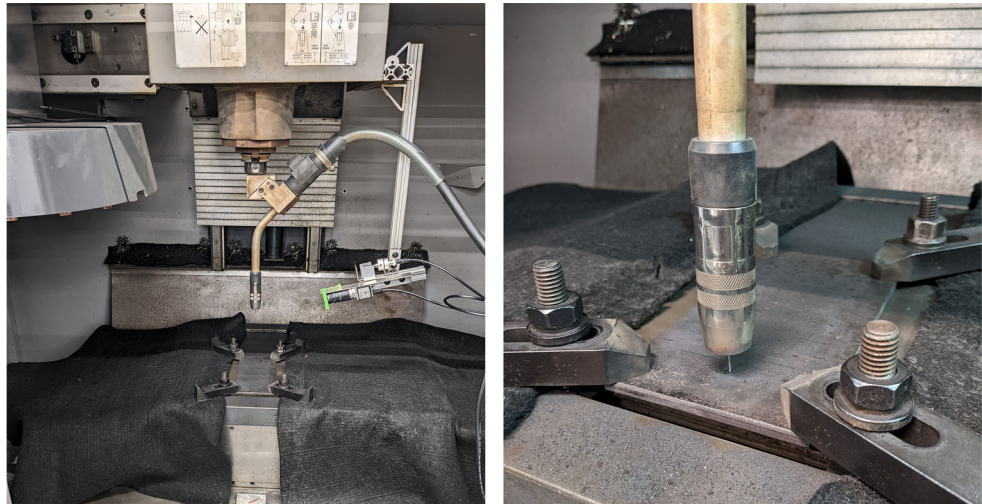


Fig. 3 Cincinnati retrofit WAAM system



by the bead overlapping method proposed by Ding et al. [18].

$$TS_{bo} = TS_y = \frac{TS_w}{n\sqrt{\left(\frac{\lambda}{4A}\right)^2 + 1}} \quad (1)$$

where

TS_{bo} = bead overlap torch speed [inch/min]

TS_y = weave traverse torch speed [inch/min]

TS_w = weave path torch speed [inch/min]

λ = weave path wavelength [inch]

A = weave path amplitude [inch]

n = number of overlapping beads

2.4 Weave experiments

2.4.1 Single-layer depositions

The single-layer weave samples were generated for a three-factor, three-level fractional factorial experiment. Sample depositions were programmed to be 3 inches long in the main build direction. The parameter levels and combinations for all samples can be seen in Table 1. For each sample, the bead penetration, height, and width were measured.

2.4.2 Multi-layer depositions

The weave wall samples were generated for a three-factor, two-level full factorial experiment. Parameters and levels

Table 1 Single-layer weave experiment parameters

Sample Name	Torch Speed [in/min]	Wavelength [in]	Amplitude [in]	TS_y [in/min]
WS 01	35	0.20	0.10	31.30
WS 02	35	0.20	0.20	33.95
WS 03	35	0.10	0.20	34.73
WS 04	35	0.10	0.10	33.95
WS 05	45	0.20	0.10	40.25
WS 06	45	0.20	0.20	43.66
WS 07	45	0.10	0.20	44.65
WS 08	45	0.10	0.10	43.66
WS 09	55	0.20	0.10	49.19
WS 10	55	0.20	0.20	53.36
WS 11	55	0.10	0.20	54.58
WS 12	55	0.10	0.10	53.36
WS 13	45	0.10	0.15	44.39
WS 14	45	0.20	0.15	42.69
WS 15	45	0.15	0.10	42.13
WS 16	45	0.15	0.20	44.23

Table 2 Multi-layer weave experiment parameters

Sample Name	Vertical Step Per Layer [in]	Interlayer Dwell Time [s]	Torch Speed [in/min]	Wavelength [in]	Amplitude [in]	Path Length [in]	Layer Time [s]
WW 1	0.08	120	35	0.20	0.10	11.2	19.2
WW 2	0.10	120	35	0.20	0.20	20.6	35.3
WW 3	0.15	180	35	0.10	0.20	40.3	69.1
WW 4	0.10	120	35	0.10	0.10	20.6	35.3
WW 5	0.08	120	55	0.20	0.10	11.2	12.2
WW 6	0.08	120	55	0.20	0.20	20.6	22.5
WW 7	0.10	180	55	0.10	0.20	40.3	44.0
WW 8	0.10	120	55	0.10	0.10	20.6	22.5

for the experiment are listed in Table 2. The vertical step per layer was decided based on the height of a single layer and was held constant to maintain a consistent contact tip to work distance throughout the build. Each wall was built with a varying number of layers with the goal to reach around 1.5 inches in height. This height was chosen to provide a larger scan area for analysis and to achieve a steady state geometry after a few initial layers. The build direction was alternated for each layer to minimize errors at the ends of the walls due to the arc stopping and starting.

2.5 Bead overlap experiments

2.5.1 Single-layer depositions

The single-layer bead overlap samples were chosen to match those of four single-layer weave samples. The parameter levels and combinations for each sample can be seen in Table 3. The overlap samples OS 1, OS 2, OS 3, and OS 4 correspond to WS 04, WS 03, WS 12, and WS 11 of the single-layer weave experiment respectively. The horizontal stepover for overlapping beads was calculated using Eq. 2 [18] and each sample was 5 inches long after deposition.

$$Step_h = 0.738w \quad (2)$$

where

$Step_h$ = horizontal stepover

w = width of a single bead

Table 3 Single-layer bead overlap experiment parameters

Sample Name	Overlapped Beads	Horizontal Step [in]	Torch Speed [in/min]
OS 1	2	0.145	16.98
OS 2	2	0.220	8.68
OS 3	2	0.131	26.68
OS 4	2	0.174	13.64

2.5.2 Multi-layer depositions

Much like for the single-layer bead overlap experiment, the samples for multi-layer bead overlap walls were chosen to match the layer deposition time of four walls from the multi-layer weave experiment. Additionally, the path parameters and length are the same as the single-layer experiment to maintain consistency and allow for easy comparison. The overlap samples OW 1, OW 2, OW 3, and OW 4 correspond to WW 4, WW 3, WW 8, and WW 7 of the multi-layer weave experiment respectively. Parameters and levels for the overlapping bead wall experiment are listed in Table 4. The same considerations for the vertical step per layer and number of layers deposited were made for the bead overlap walls as was made for the weave walls. Similarly, the interlayer dwell time was maintained between direct comparisons, and the build direction was alternated every layer.

2.6 Data acquisition and analysis

The penetration depth, bead height, and bead width of single-layer samples, exemplified in Fig. 4, were determined via the built-in measuring tools on the microscope software. For the multi-layer experiments, the samples were scanned with a laser light scanner and the data was used to generate a watertight STL file. The STLs were imported into MATLAB and used to populate a dataset of X,Y,Z coordinates defining the feature. First, the dataset for each build was cropped to remove any data points generated from scanning the substrate. A copy of the dataset was made and data points correlating to the top surface of the wall are cropped from this new dataset. Next, both datasets were split into 40 sections of equal length along the main build direction (Y-axis). Each section was treated as a separate sample for the given parameter set associated with the build as a whole. Given that the walls are all approximately 4 inches long after preparation, each of the 40 samples is approximately 0.1 inches in length. This size consists of enough data

Table 4 Multi-layer bead overlap experiment parameters

Sample Name	Overlapped Beads	Horizontal Step [in]	Vertical Step Per Layer [in]	Interlayer Dwell Time [s]	Torch Speed [in/min]
OW 1	2	0.145	0.08	120	16.98
OW 2	2	0.220	0.10	180	8.68
OW 3	2	0.131	0.07	120	26.68
OW 4	2	0.174	0.08	180	13.64

points to act as a slice of the wall and offers an accurate representation of the total wall geometry. An example of a series of wall sections after cropping is shown in Fig. 5.

2.6.1 Geometry evaluation metrics

After digitally sectioning, the dataset with the top and bottom cropped was divided into two halves. Each half was associated with one side surface of the wall. For the calculation of surface form error, planes were fit to each surface, and the orthogonal deviation of each point on the surface to the plane was calculated. The form error of each wall surface was then calculated as the distance between the two points furthest from each other in the direction of the plane normal vector. The total wall form error was then calculated by taking an average of the individual side surface form errors.

Additionally, through analysis of the wall surfaces, the wall's effective width (EW) was calculated. As surface misalignment does not allow for form error to be directly used to calculate the EW, it was obtained using the minimum and maximum bounds of the wall surfaces in the transverse build direction. Therefore, the distance from the minimum point of the right wall surface and the maximum point of the left wall surface constitute the EW. Similarly, the distance from the maximum point of the right surface and the minimum point of the left surface constitutes the total wall width. The ratio of the effective width to the

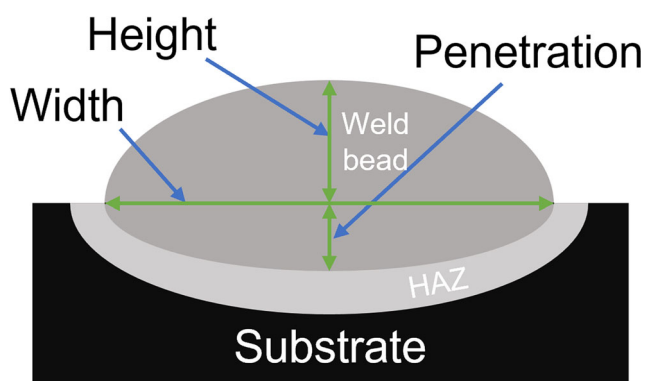


Fig. 4 Measurement of single-layer bead penetration depth, bead height, and bead width

total width, or width ratio (WR), is a useful metric to compare the effects of the process parameter set on the total manufacturing efficiency with respect to the amount of post deposition machining required to obtain smooth wall surfaces. This ratio was also used to compare the walls produced with a weave path to those produced with overlapping beads. Figure 6 depicts how the width of wall profiles are calculated, where the red vertical lines bound the effective wall width and the green vertical lines bound the wall at maximum width.

Another metric important to additive manufacturing (AM) is layer height. To determine the effects of weave path parameters on the complete geometry of WAAM walls, the effective height per deposited layer was also calculated. As seen in Fig. 6, the effective layer height is the total effective wall height divided by the number of layers required to build the sample.

The efficiency of AM strategies and process parameters is often also considered in the context of time. Therefore, the last metric used to compare the parameter levels and path strategies for this study was the effective volumetric

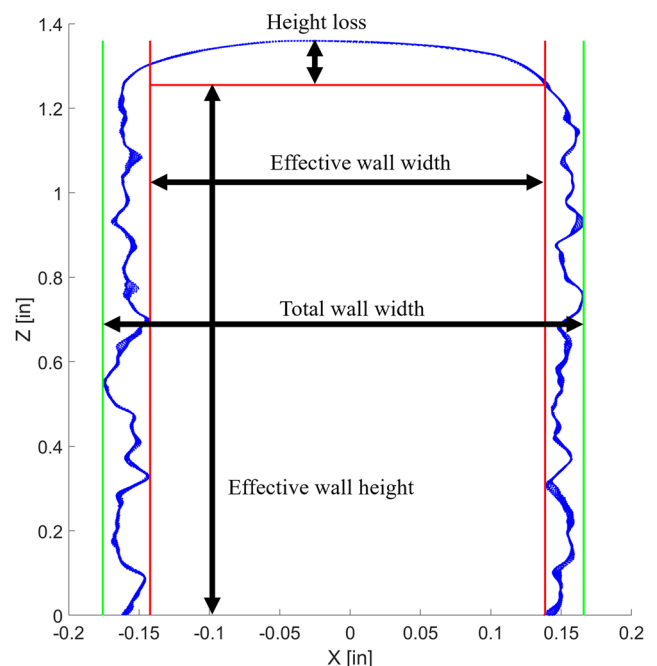


Fig. 6 Depiction of wall section widths and height

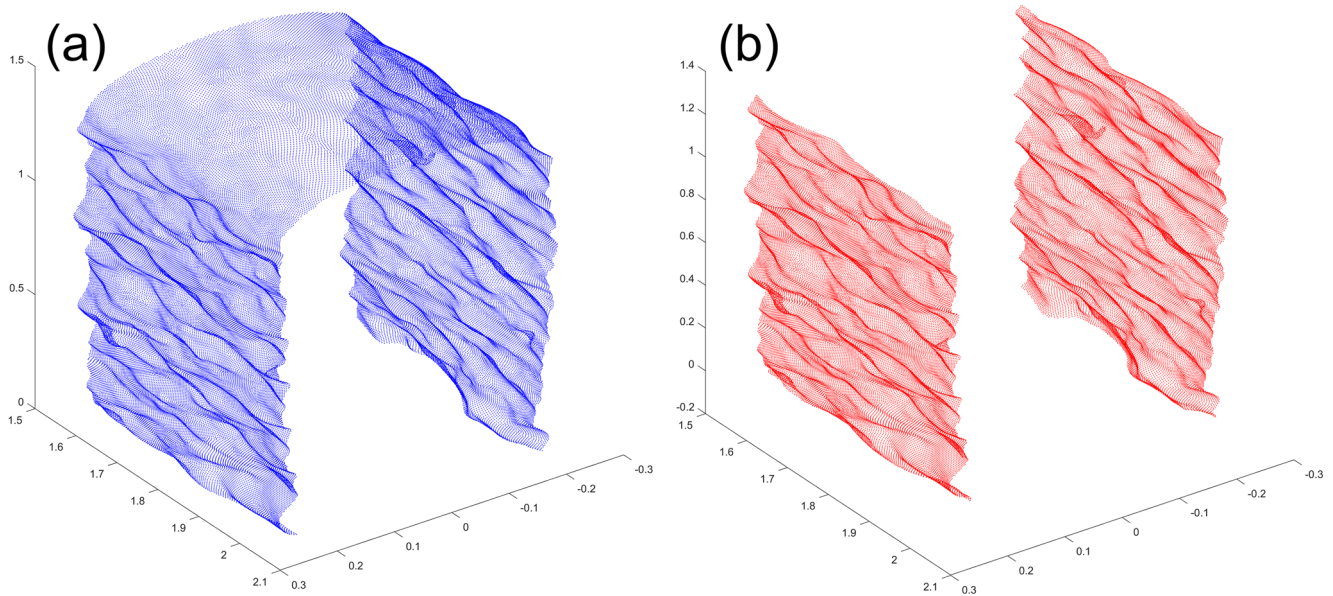


Fig. 5 Plots of wall section point cloud data. (a) Data with only substrate cropped. (b) Data with top surface and substrate cropped

deposition rate (EVDR). The EVDR is defined as the volume of usable material deposited per minute and was calculated using Eq. 3.

$$EVDR = \frac{UHPL * UW * BL}{t_{layer}} * 60 \tag{3}$$

where

$UHPL$ = effective height per layer [inch]

UW = effective wall width [inch]

BL = bead length [inch]

t_{layer} = layer time [s]

3 Results and discussion

3.1 Single-layer depositions

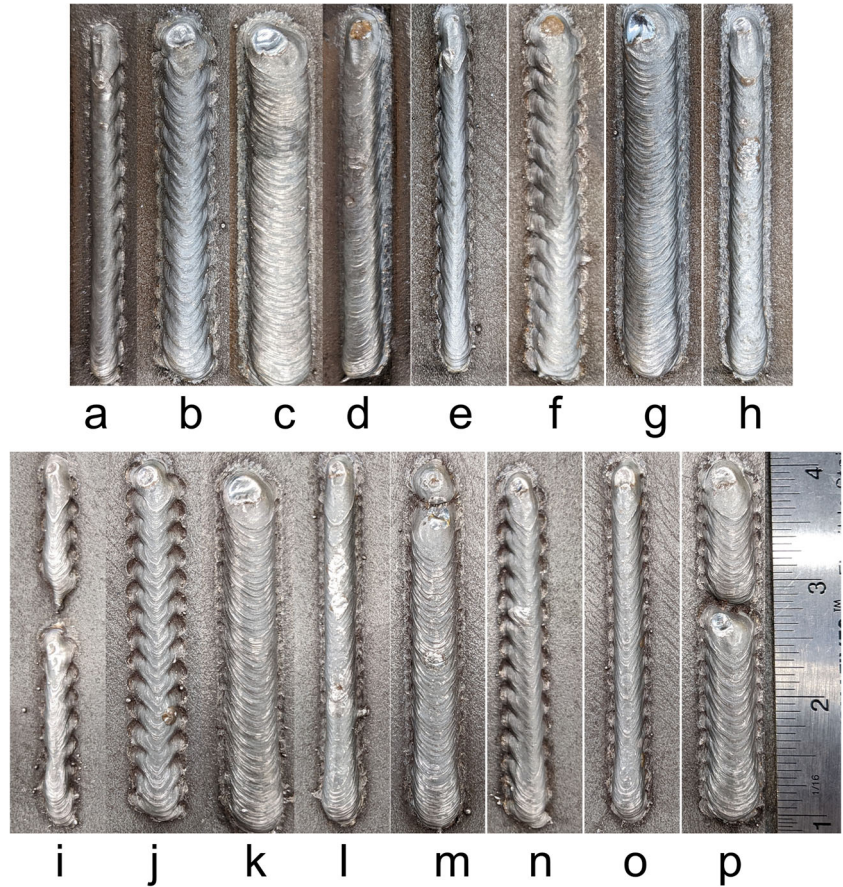
The as-deposited single-layer weave samples are shown in Fig. 7. The discontinuities in some samples were the result of an arc failure occurring during the deposition. The dramatic change in bead profiles between the samples with varying process parameters can be easily seen. The cross-sectional bead geometry and microstructure of a few weave samples are shown in Fig. 8. Here, the microstructure consists of large columnar grains oriented in the direction parallel to the feed wire.

From the results, it was found that only TS had a significant effect on bead penetration, and the relationship can be seen in Fig. 9(a). The lack of a significant effect

from λ and A on penetration can be partially attributed to only having two levels for these parameters. Additionally, torch paths with transverse arc motion have been shown to produce consistently shallow penetration rather than the deep finger penetration of unidirectional arc paths because the arc heat is distributed orthogonal to the main direction of travel [8]. These results align with what has been seen in the literature as arc rotation [19] and laser-MAG weaving [20] resulted in more shallow penetration when compared to linear paths. Also, it has been observed that the largest contributor to penetration is welding current [21] which was held constant in this study by maintaining a constant power and WFS.

It was also found that λ had the greatest effect on the bead height. The observed trend shown in Fig. 9(b) is a linear relationship where increasing λ resulted in a decreasing bead height. This is due to less material being deposited in the same relative location per unit time with a higher λ . Similarly, A had the most significant effect on the bead width, as this parameter has a direct influence on material deposition orthogonal to the primary layer deposition direction. As A increased, the bead width also increased; this relationship is shown in Fig. 9(c). The second most influential parameter on resulting bead width was λ , where in Fig. 9(d), it can be seen that bead width decreased with an increasing λ . This relationship can be explained by the effect λ has on the transverse TS. While overall TS did not seem to have an effect on the bead width, shorter λ s decreased the TS_x . A lower TS_x resulted in the arc dwelling at the apex of the weave path for longer amounts of time. This effect caused more material to be deposited on the edges of the bead, therefore, making it wider.

Fig. 7 Single-layer depositions. (a) WS 01. (b) WS 02. (c) WS 03. (d) WS 04. (e) WS 05. (f) WS 06. (g) WS 07. (h) WS 08. (i) WS 09. (j) WS 10. (k) WS 11. (l) WS 12. (m) WS 13. (n) WS 14. (o) WS 15. (p) WS 16

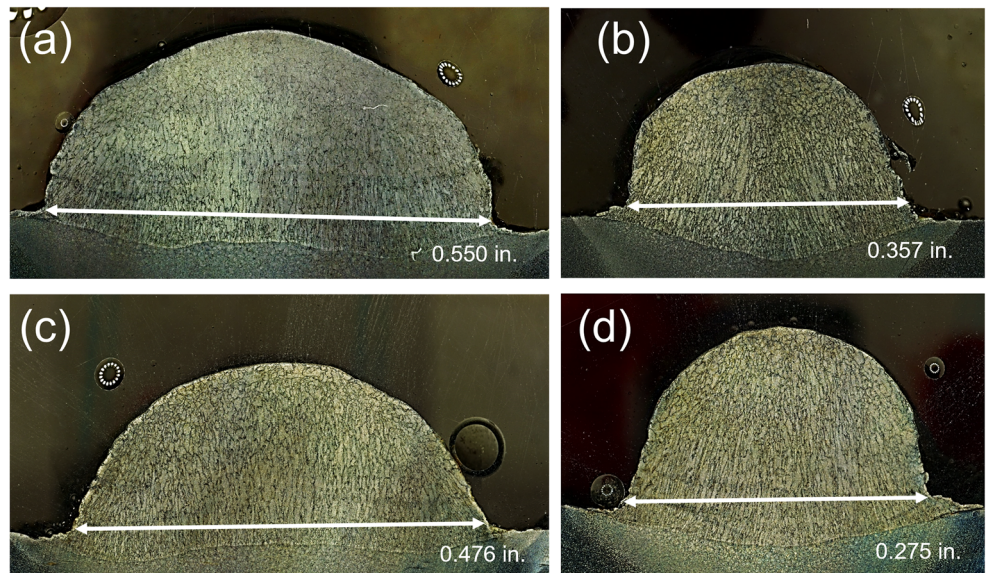


3.1.1 Comparison of single-layer weave beads to overlapping beads

A comparison between weld penetration, maximum bead height, and deposition width was made between the

single-layer weave and bead overlap experiments. The as-deposited bead overlap samples can be seen in Fig. 10. The comparison of measurement data is shown in Fig. 11, where the data is ordered from left to right in increasing sample deposition time, and a negative percent difference indicates

Fig. 8 Single-layer weave bead profiles and microstructure. (a) WS 03. (b) WS 04. (c) WS 11. (d) WS 12



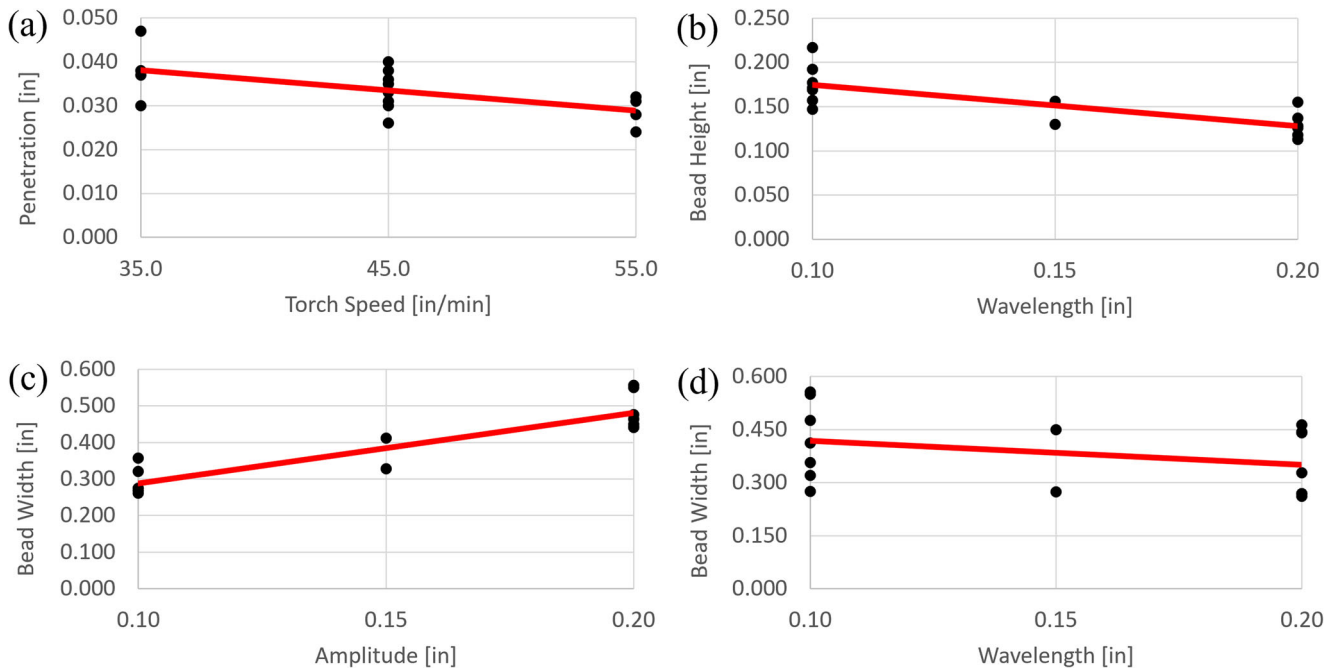


Fig. 9 Effects of path parameters on single-layer geometry. (a) TS vs Bead Penetration. (b) λ vs. Bead Height. (c) A vs. Bead Width. (d) λ vs. Bead Width

the measurement from the weave sample is smaller than that of the bead overlap sample. As the comparisons are only made between weave samples with a constant λ , the main contributor to deposition time here is amplitude. Therefore, the two bars on the right represent a comparison to weave samples with the high amplitude setting ($A = 0.2$ inches).

The comparisons show a decrease in penetration from OS 2 to WS 03 and from OS 4 to WS 11 by 56.3% and 31.6% respectively. This effect can be attributed to the very low TS required for the overlap samples to match the TS_y of the weave samples. As described previously, low TSs resulted in deeper penetration. It is also evident from the sample cross sections in Fig. 8

that the penetration profiles of the weave samples were more hemispherical and uniform compared to the deep, finger-type penetration of the bead overlap samples seen in Fig. 12. An increase in bead height by 1.9–17.0% from OS to WS across all sample comparisons was observed. Also from the deposition cross sections, it is evident that the weave samples had a significantly flatter and more uniform top surface which would lead to the bead overlap samples requiring more finishing, further reducing their heights. Additionally, it can be seen that the weave samples had a homogeneous columnar grain structure whereas the microstructure of the bead overlap samples was interrupted at the joint location between the two beads. In all bead overlap samples, the heat-affected zone of the second bead had changed the microstructure of the first bead from large columnar grains to smaller, equiaxed grains. The observed effects on microstructure are consistent with the findings of Aldalur et al. [17] who showed that a heterogeneous microstructure occurs in walls built with overlapping beads, and walls built with a weaving path generate a homogeneous microstructure.

The only factor affecting deposition time of the bead overlap path was TS, where lower TS increased the deposition time. On the other hand, the deposition time of weave samples was affected by λ , TS, and A . Figure 11(a) shows deeper penetration for bead overlap samples compared to the weave samples with increasing deposition time. Similarly, the sample comparisons from Fig. 11(b) show smaller bead widths for weave samples

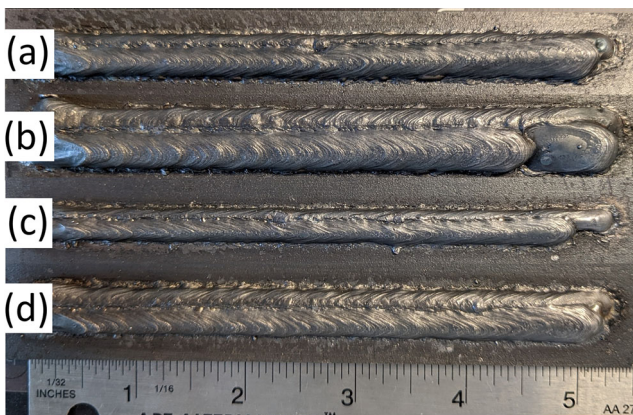


Fig. 10 Single-layer bead overlap depositions. (a) OS 1. (b) OS 2. (c) OS 3. (d) OS 4

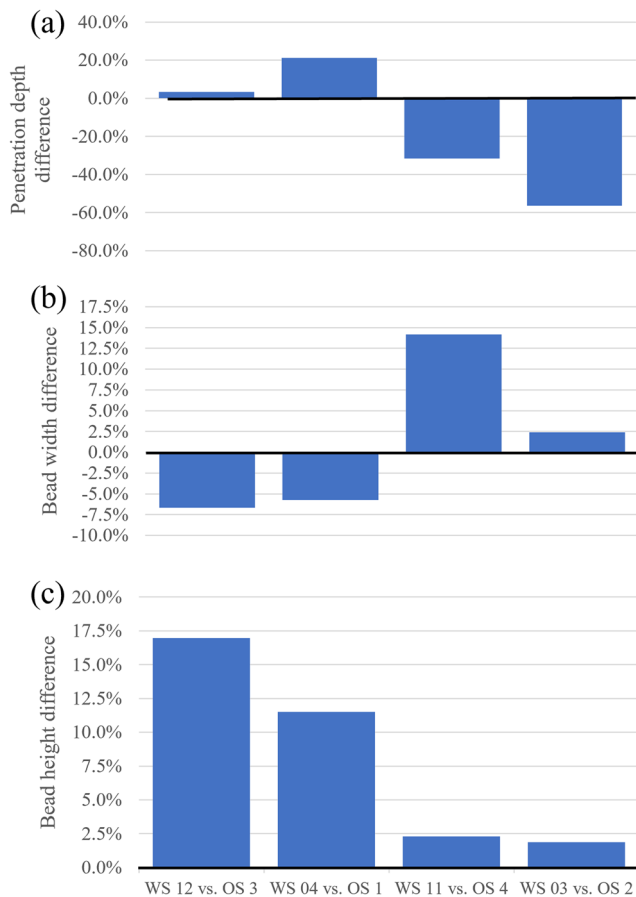


Fig. 11 Comparison of single-layer weave beads to overlapping beads. (a) Difference between penetration depth. (b) Difference between bead width. (c) Difference between bead height

at shorter deposition times, but outgrow their overlap counterparts at longer deposition times. Finally, Fig. 11(c) shows a positive difference in bead height for the weave path across all samples, but the effect decreased with larger amplitudes.

3.2 Multi-layer depositions

The multi-layer weave path samples can be seen in Fig. 13. Visually, there is an obvious difference in surface quality between the samples. For example, sample WW 5 (Fig. 13(e)) exhibits a seemingly poor surface finish while sample WW 2 (Fig. 13(b)) shows a much more smooth surface finish and an external pattern can be seen on the surface as a result of the weave path.

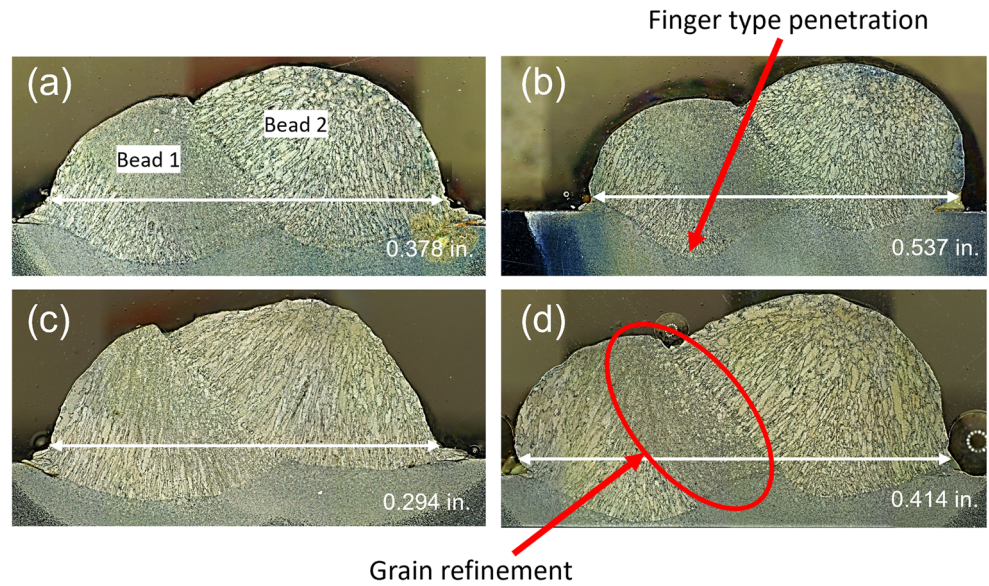
The most significant changes in geometry were due to the effects of all main parameters on effective width, effective layer height, and form error. The influence of parameters on effective width can be seen in Fig. 14 with the standard deviation of measurements as error bars. The results show a clear increase in effective width with a decrease in TS

and λ , and with an increase in A . A higher TS resulted in an average loss of 0.053 inches in effective width (17%), while the higher λ setting resulted in an average decrease of 0.085 inches (29%). The most dramatic effect resulted from an increase in the A , where the effective width grew by an average of 0.178 inches (42%). The effect of A follows from the single-layer experimental results and makes sense intuitively as changes to the parameter directly influenced the deposition of material orthogonal to the main deposition direction. Similarly, lower TS and λ caused a dramatic decrease in TS_y which resulted in more material being deposited in a single location along the build direction, thus creating a radially larger melt pool.

The influence of the main parameters on effective layer height can be seen in Fig. 15, with the standard deviation of measurements as error bars. The results show a clear increase in height with a decrease in TS and λ , and with an increase in A . Increasing the TS from 35 inches/min to 55 inches/min led to an average ELH loss of 0.027 inches (37%). Similarly, the higher λ level led to an average decrease in ELH of 0.038 inches (55%). Lastly, the samples produced with higher A had an average ELH increase of 0.016 inches (16%). Furthermore, sample WW 3 represents the combination of parameters that produced the largest layer height of 0.140 inches, while WW 5 represents the parameter set that produced the smallest layer height at 0.056 inches, a difference of 0.084 inches. Although these walls had the maximum and minimum layer times respectively, WW 3 exhibited a 22% higher EVDR. These effects follow the relationships observed in the single-layer experiments. Interestingly, the effect of A was more obvious at lower λ s and can be attributed to the lack of available area for melt pool spreading in this configuration. When the λ was larger, a gap was created between the sides of the previously solidified bead section and the newly deposited material, allowing the molten material to spread out horizontally rather than accumulate as increased height.

As mentioned previously, the wall surface quality differed significantly across samples, which indicates large variation in form error. From the results shown in Fig. 16, the A and interaction between TS and λ had a clear effect on the form error. The higher A level resulted in larger form errors across all other parameter settings by an average of 0.01 inches. Additionally, form error was largest at the combinations of high TS and low λ s, and smallest with combinations of low TSs and large λ s. This relationship can be attributed to generally larger feature sizes produced with low TS and small λ , as form error would scale with feature size. Also, the gaps created by large λ s resulted in larger form error, but could be more easily filled when A was larger or with lower TSs. However, when TS and λ were both low, the gaps could be overfilled and result in excess horizontal material spread, exaggerating the stair stepping

Fig. 12 Single-layer overlap bead profiles and microstructure. (a) OS 1. (b) OS 2. (c) OS 3. (d) OS 4



effect inherent to AM processes and associated with high form error.

3.2.1 Comparison of multi-layer weave walls to overlapping bead walls

The multi-layer bead overlap strategy samples can be seen in Fig. 17. For these samples, the indicators of build quality are the size of layer overlap and large-scale defects like those apparent in the first few layers of OW 2 (Fig. 17(b)). A comparison of weave wall geometry metrics to their bead overlap counterparts is shown in Fig. 18 where the

bars are ordered from left to right by increasing deposition time. From the comparison, the ELHs, WRs, and EVDRs for weave builds were generally higher while the average form error was lower across all weave samples as seen in Fig. 18(a), (b), (c), (d). The elevated ELH of the weave samples follows the results from the single bead depositions where the weave beads were found to have flatter tops, thus less height loss between the maximum height and effective height. The ELH advantage of weave walls stems from this reduction in height loss of the final layer. As for the differences in WR and form error which manifest in higher EVDRs for weave samples, the exact mechanism is

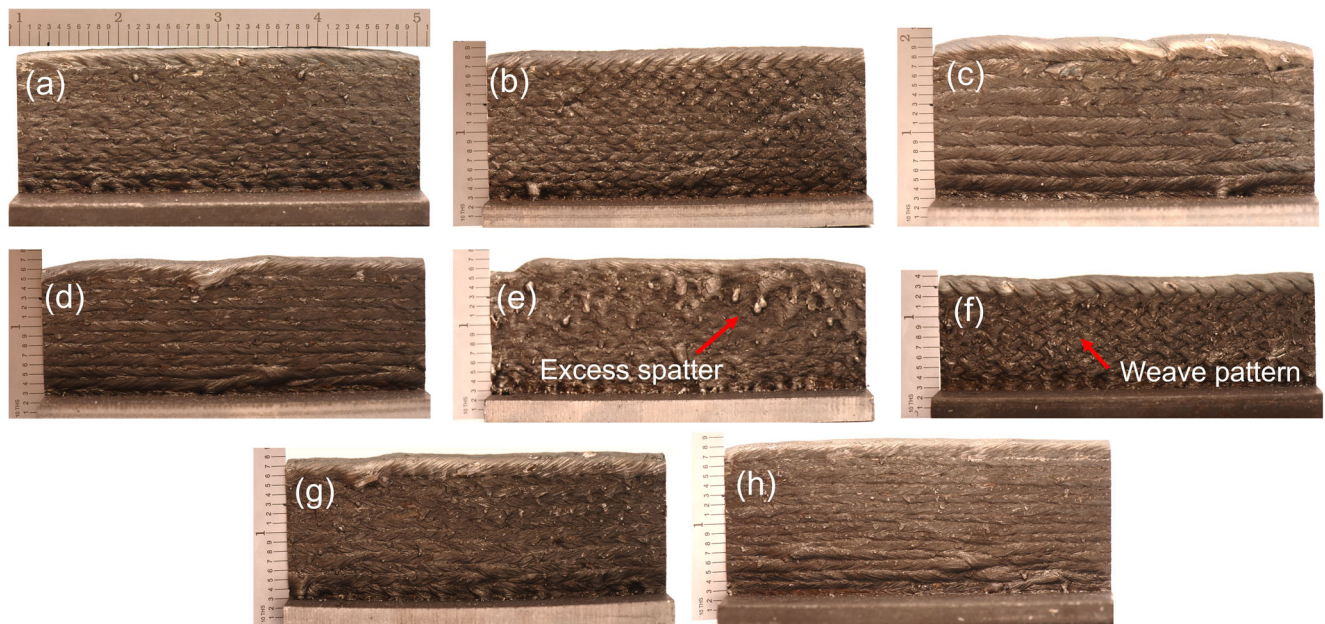


Fig. 13 Multi-layer weave deposition experiments. (a) WW 1. (b) WW 2. (c) WW 3. (d) WW 4. (e) WW 5. (f) WW 6. (g) WW 7. (h) WW 8

Fig. 14 Effective weave wall width vs. parameters. (a) $\lambda = 0.2, A = 0.1$. (b) $\lambda = 0.2, A = 0.2$. (c) $\lambda = 0.1, A = 0.2$. (d) $\lambda = 0.1, A = 0.1$. (e) TS = 35, A = 0.1. (f) TS = 35, A = 0.2. (g) TS = 55, A = 0.2. (h) TS = 55, A = 0.1. (i) TS = 35, $\lambda = 0.1$. (j) TS = 35, $\lambda = 0.2$. (k) TS = 55, $\lambda = 0.2$. (l) TS = 55, $\lambda = 0.1$

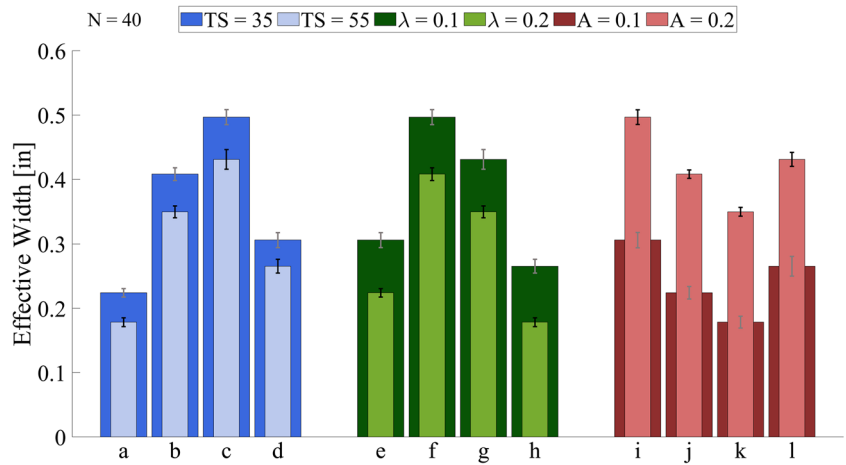


Fig. 15 Effective weave wall layer height vs. parameters. (a) $\lambda = 0.2, A = 0.1$. (b) $\lambda = 0.2, A = 0.2$. (c) $\lambda = 0.1, A = 0.2$. (d) $\lambda = 0.1, A = 0.1$. (e) TS = 35, A = 0.1. (f) TS = 35, A = 0.2. (g) TS = 55, A = 0.2. (h) TS = 55, A = 0.1. (i) TS = 35, $\lambda = 0.1$. (j) TS = 35, $\lambda = 0.2$. (k) TS = 55, $\lambda = 0.2$. (l) TS = 55, $\lambda = 0.1$

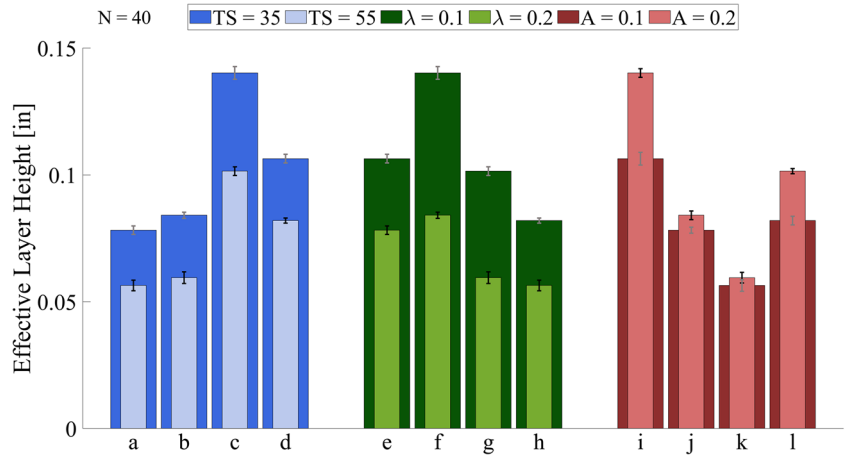
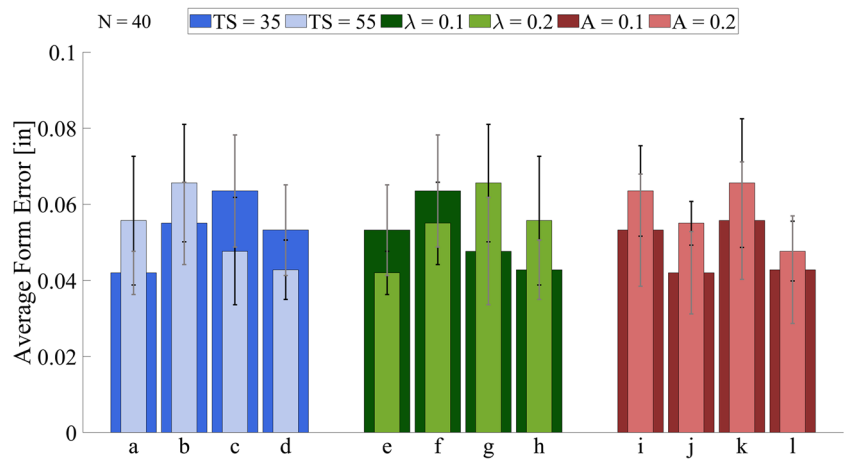


Fig. 16 Average side wall form error vs. parameters. (a) $\lambda = 0.2, A = 0.1$. (b) $\lambda = 0.2, A = 0.2$. (c) $\lambda = 0.1, A = 0.2$. (d) $\lambda = 0.1, A = 0.1$. (e) TS = 35, A = 0.1. (f) TS = 35, A = 0.2. (g) TS = 55, A = 0.2. (h) TS = 55, A = 0.1. (i) TS = 35, $\lambda = 0.1$. (j) TS = 35, $\lambda = 0.2$. (k) TS = 55, $\lambda = 0.2$. (l) TS = 55, $\lambda = 0.1$



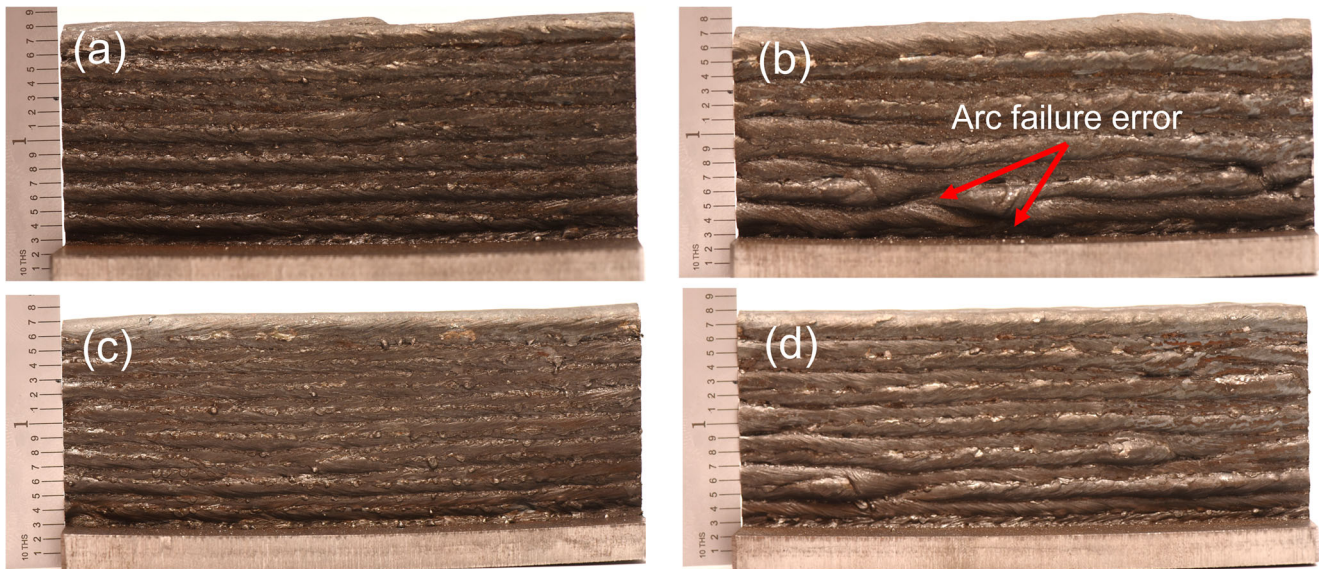


Fig. 17 Multi-layer bead overlap deposition experiments. (a) OW 1. (b) OW 2. (c) OW 3. (d) OW 4

unknown and requires further investigation. However one explanation for the higher WR of weave samples is that the individual beads that compose a layer have a taller and more narrow profile compared to the overlapped beads. This causes the weave bead to stack more efficiently and have less material droop off the side of the wall, resulting in less dramatic form undulations on the surface. Similarly, the weave walls may have less form error because their

weaving deposition pattern constricts transverse metal flow, hindering deviations that would otherwise result in poor surface finish.

The weave samples provided the most beneficial differences at the higher deposition times (highest A). Specifically, samples WW 3 and WW 7 exhibited an increase in effective width of 10.7% and 1.8% (Fig. 18(e)), a decrease in form error by 36.9% and 46.1%, and a gain in

Fig. 18 Comparison of multi-layer weave walls to overlapping bead walls. (a) Difference in effective layer height. (b) Difference in width ratio. (c) Difference in EVDR. (d) Difference in form error. (e) Difference in effective width

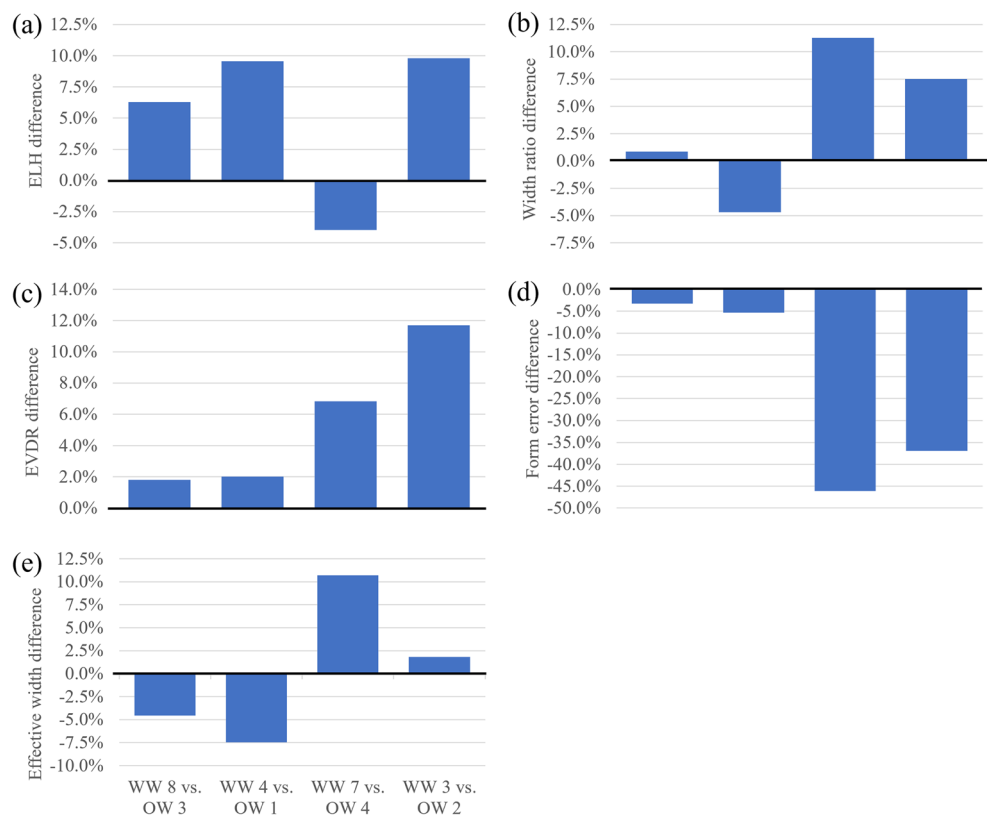
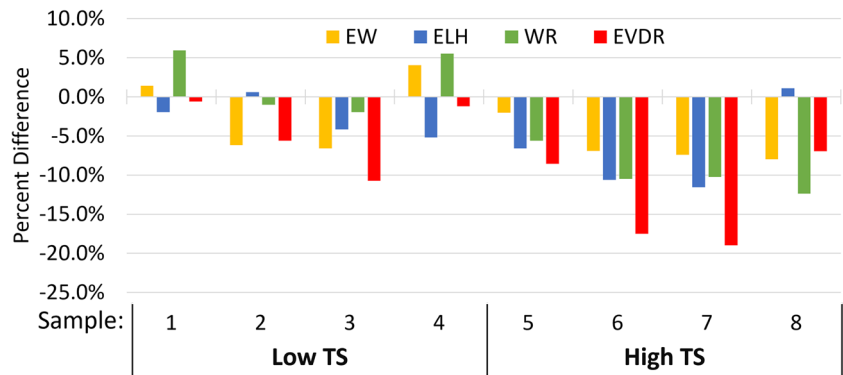


Fig. 19 Weave wall geometry comparison: 0° vs. 180° layer phase offset



EVDR of 11.7% and 6.8% respectively over their overlap counterparts. These samples were both deposited at the high A level which proves the main advantage of weave is its ability to produce more usable material when the feature size is large. With additional experiments, it is expected that weave paths with higher *As* would continue to provide higher EVDRs than what is possible with an increasing number of overlapping beads. Likewise, an increase in EVDR across all samples indicates an advantage for using a weave torch path strategy over an overlapping bead strategy for constructing WAAM features.

3.2.2 Influence of layer phase offset in weave experiments

An additional experiment was performed to determine the influence of adding a phase offset for alternating weave path layers on the geometry of WAAM walls. This experiment considered samples with duplicated path parameters for all eight multi-layer weave wall samples, with the addition of a 180° phase offset for alternating layers. The results of a comparison between walls with 0° phase and those with 180° phase offset can be seen in Fig. 19. Here, a negative percent difference indicates the average measured value for a wall with no layer phase offset is less than that of the wall with 180° layer phase offset. From the data it is evident that in general, the 0° phase samples deposited at the lower TS had a higher total width than their 180° phase shifted counterparts. All 0° phase samples except WW 1 and WW 4 had an increased effective width of 2.06–8.32%. Additionally, all 0° phase samples except WW 2 and WW 8 had higher effective layer heights than the 180° phase samples by 1.96–12.28%. For samples with higher TSs, the 0° phase samples performed the best with respect to the width ratio, showing an increase of 8.93–20.96%. Finally, all 0° phase samples exhibited an increase in the effective volumetric deposition rate of 0.59–20.96%. Similar to how the weave path provides geometric enhancements over overlapping beads via creating a guided flow path for the metal, maintaining this pattern every layer versus disrupting it shows similar results.

4 Conclusions

This work presents an approach to increase the manufacturability of large features produced with WAAM. Currently, there is a lack of control of the geometry and quality of WAAM features produced with standard torch path strategies. The application of novel torch path strategies has not been investigated as a means to reduce geometric errors and thus overall manufacturing time. In this work, the use of a weaving torch path was evaluated with respect to the geometry of features produced with varying levels of torch speed, wavelength, and amplitude. The geometries of as-built features were compared to those of features produced with a standard overlapping bead model. Additionally, the implementation of a phase offset for a weave waveform was evaluated. The results of this study developed an improved understanding of how the use of a weaving path and the associated parameter levels directly impact the feature size and surface quality. The major findings of this study are as follows:

- Penetration depth of weave depositions decreases with increasing torch speed and remains relatively constant as deposition time increases.
- Larger effective wall widths and layer heights can be produced with larger amplitudes, smaller wavelengths, and lower torch speeds.
- Smaller amplitudes and the combination of a low torch speed with a high wavelength results in lower form error of the side surfaces of WAAM walls.
- The total and effective widths of weave and bead overlap walls grow at relatively the same rate with respect to deposition time.
- The use of a weave path can reduce the side surface form error by 3.2–46.1% over bead overlap walls.
- Deposition time has relatively no effect on the form error of walls built with a weave path.
- The width ratio of walls can be increased by up to 11.3% by using a weave path.

- The use of a weave path strategy can improve the effective volumetric deposition rate by 1.8–11.7% compared to using an overlapping bead strategy.
- Implementing a 180° phase shift in the waveform of alternating weave layers reduces the effective wall width and effective layer height, and thus reduces the effective volumetric deposition rate in most cases.

Acknowledgements Thank you to Jaime Berez (Georgia Institute of Technology) for providing self-developed MATLAB tools that aided in the metrology and analysis portion of this research.

Author contribution Conceptualization: Jacob Bultman, Christopher Saldana. Methodology: Jacob Bultman. Validation: Jacob Bultman, Christopher Saldana. Analysis: Jacob Bultman. Writing — original draft: Jacob Bultman. Writing — review and editing: Christopher Saldana. Funding acquisition: Christopher Saldana. All authors have read and agreed to the published version of the manuscript.

Funding This work was supported by the US Department of Energy DE-EE0008303

Data Availability All data is available upon request to the corresponding author

Declarations

Conflict of interest The authors declare no competing interests

References

- Williams SW, Martina F, Addison AC et al (2016) Wire + arc additive manufacturing. *Mater Sci Technol* 32(7):641–647. <https://doi.org/10.1179/1743284715Y.0000000073>
- Ding D, Pan Z, Cuiuri D et al (2015) Wire-feed additive manufacturing of metal components: technologies, developments and future interests. *Int J Adv Manuf Technol* 81(1):465–481. <https://doi.org/10.1007/s00170-015-7077-3>
- Yang D, Wang G, Zhang G (2017) Thermal analysis for single-pass multi-layer GMAW based additive manufacturing using infrared thermography. *J Mater Process Technol* 244:215–224. <https://doi.org/10.1016/j.jmatprotec.2017.01.024>
- Colegrove PA, Coules HE, Fairman J et al (2013) Microstructure and residual stress improvement in wire and arc additively manufactured parts through high-pressure rolling. *J Mater Process Technol* 213(10):1782–1791. <https://doi.org/10.1016/j.jmatprotec.2013.04.012>
- Fuchs C, Baier D, Semm T et al (2020) Determining the machining allowance for WAAM parts. *Prod Eng* 14(5):629–637. <https://doi.org/10.1007/s11740-020-00982-9>
- Jafari D, Vaneker THJ, Gibson I (2021) Wire and arc additive manufacturing: Opportunities and challenges to control the quality and accuracy of manufactured parts. *Mater Des* 202:109,471. <https://doi.org/10.1016/j.matdes.2021.109471>
- Hu JF, Yang JG, Fang HY et al (2006) Numerical simulation on temperature and stress fields of welding with weaving. *Sci Technol Weld Join* 11(3):358–365. <https://doi.org/10.1179/174329306X124189>
- Chen Y, He Y, Chen H et al (2014) Effect of weave frequency and amplitude on temperature field in weaving welding process. *The Int J Adv Manuf Technol* 75(5-8):803–813. <https://doi.org/10.1007/s00170-014-6157-0>
- He T, Yu S, Runzhen Y et al (2022) Oscillating wire arc additive manufacture of rocket motor bimetallic conical shell. *The International Journal of Advanced Manufacturing Technology* <https://doi.org/10.1007/s00170-021-08477-2>
- Yaseer A, Chen H (2021) Machine learning based layer roughness modeling in robotic additive manufacturing. *J Manuf Process* 70:543–552. <https://doi.org/10.1016/j.jmapro.2021.08.056>
- Ma G, Zhao G, Li Z et al (2019a) A path planning method for robotic wire and arc additive manufacturing of thin-walled structures with varying thickness. *IOP Conf Series: Mater Sci Eng* 470:012,018. <https://doi.org/10.1088/1757-899X/470/1/012018>
- Ma G, Zhao G, Li Z et al (2019b) Optimization strategies for robotic additive and subtractive manufacturing of large and high thin-walled aluminum structures. *Int J Adv Manuf Technol* 101(5-8):1275–1292. <https://doi.org/10.1007/s00170-018-3009-3>
- Zhan X, Zhang D, Liu X et al (2017a) Comparison between weave bead welding and multi-layer multi-pass welding for thick plate Invar steel. *Int J Adv Manuf Technol* 88(5):2211–2225. <https://doi.org/10.1007/s00170-016-8926-4>
- Zhan X, Liu X, Wei Y et al (2017b) Microstructure and property characteristics of thick Invar alloy plate joints using weave bead welding. *J Mater Process Technol* 244:97–105. <https://doi.org/10.1016/j.jmatprotec.2017.01.014>
- Guzman-Flores I, Vargas-Arista B, Gasca-Dominguez JJ et al (2017) Effect of torch weaving on the microstructure, tensile and impact resistances, and fracture of the HAZ and weld bead by robotic GMAW process on ASTM a36 steel. *Soldagem & Inspeção* 22:72–86. <https://doi.org/10.1590/0104-9224/SI2201.08>
- Aldalur E, Veiga F, Suárez A et al (2020a) Analysis of the wall geometry with different strategies for high deposition wire arc additive manufacturing of mild steel. *Metals* 10(7):892. <https://doi.org/10.3390/met10070892>
- Aldalur E, Veiga F, Suárez A et al (2020b) High deposition wire arc additive manufacturing of mild steel: Strategies and heat input effect on microstructure and mechanical properties. *J Manuf Process* 58:615–626. <https://doi.org/10.1016/j.jmapro.2020.08.060>
- Ding D, Pan Z, Cuiuri D et al (2015) A multi-bead overlapping model for robotic wire and arc additive manufacturing (WAAM). *Robot Comput Integr Manuf* 31:101–110. <https://doi.org/10.1016/j.rcim.2014.08.008>
- Rao PS, Gupta OP, Murty SSN (2004) A study on the weld bead characteristics in pulsed gas metal arc welding with rotating arc. In: 23rd International Conference on Offshore Mechanics and Arctic Engineering, Volume 2. ASMEDE, pp 953–957. <https://doi.org/10.1115/OMAE2004-51580>
- Cai C, Li L, Chen X et al (2016) Study on laser-MAG hybrid weaving welding characteristics for high-strength steel. *J Laser Appl* 28(2):022,401. <https://doi.org/10.2351/1.4944095>
- Karadeniz E, Ozsarac U, Yildiz C (2007) The effect of process parameters on penetration in gas metal arc welding processes. *Mater Des* 28(2):649–656. <https://doi.org/10.1016/j.matdes.2005.07.014>

Publisher's note Springer Nature remains neutral with regard to jurisdictional claims in published maps and institutional affiliations.

Springer Nature or its licensor (e.g. a society or other partner) holds exclusive rights to this article under a publishing agreement with the author(s) or other rightsholder(s); author self-archiving of the accepted manuscript version of this article is solely governed by the terms of such publishing agreement and applicable law.